Scale-Dependent Friction-Coverage Relations and Non-Local Dissipation in Surfactant Monolayers

Hongyu Gao,[†,§] James P. Ewen,[*,‡,§] Remco Hartkamp,[¶] Martin H. Müser,[†] and Daniele Dini[‡]

†*Department of Materials Science and Engineering, Universität des Saarlandes, 66123 Saarbrücken, Germany*

‡*Department of Mechanical Engineering, Imperial College London, London SW7 2AZ, UK*

¶*Process and Energy Department, Delft University of Technology, Leeghwaterstraat 39, 2628 CB Delft, The Netherlands*

§*H.G. and J.P.E. contributed equally*

E-mail: j.ewen@imperial.ac.uk

Abstract

Surfactant molecules, known as organic friction modifiers (OFMs), are routinely added to lubricants to reduce friction and wear between sliding surfaces. In macroscale experiments, friction generally decreases as the coverage of OFM molecules on the sliding surfaces increases; however, recent nanoscale experiments with sharp atomic force microscopy (AFM) tips have shown increasing friction. To elucidate the origin of these opposite trends, we use nonequilibrium molecular dynamics (NEMD) simulations and study kinetic friction between OFM monolayers and an indenting nanoscale asperity. For this purpose, we investigate various coverages of stearamide OFMs on iron oxide surfaces and silica AFM tips with different radii of curvature. We show that the differences between the friction-coverage relations from macroscale and nanoscale

experiments are due to molecular plowing in the latter. For our small tip radii, the friction coefficient and indentation depth both have a non-monotonic dependence on OFM surface coverage, with maxima occurring at intermediate coverage. We rationalise the non-monotonic relations through a competition of two effects (confinement and packing density) that varying the surface coverage has on the effective stiffness of the OFM monolayers. We also show that kinetic friction is not very sensitive to the sliding velocity in the range studied, indicating that it originates from instabilities. Indeed, we find that friction predominately originates from plowing of the monolayers by the leading edge of the tip, where gauche defects are created, while thermal dissipation is mostly localised in molecules towards the trailing edge of the tip, where the chains return to a more extended conformation.

Introduction

Nanometer-thick surfactant films adsorbed on solid surfaces are important to maintaining the effective operation of many engineering systems. Such films are particularly critical to mitigate against generally deleterious phenomena such as friction,[1] corrosion,[2] and nanoparticle agglomeration.[3] In tribology, surfactant films are formed from organic friction modifiers (OFMs), which are added to lubricants to reduce friction and wear between sliding surfaces.[4] Carboxylic acid, amine, amide, or ester surfactants with alkyl tailgroups in the range C_{12}–C_{20} are usually employed for this purpose. OFMs are particularly important in the boundary lubrication regime, where the load is primarily supported by contacting solid asperities rather than by the liquid lubricant. In lubricated machine components, the boundary regime occurs at low sliding velocity, v_s, and high pressure, P, or when lubricants with low viscosity, η, are used. Over the last few decades, lubricant viscosity has been progressively reduced to minimise energy losses from hydrodynamic friction. This means that a greater number of lubricated machine components operate under boundary lubrication conditions, making additives that reduce friction and wear in this regime increasingly important to improve energy

efficiency and to ensure reliable operation.[5]

To rationally design improved lubricant additive molecules, a detailed understanding of the atomic-scale behaviour governing their macroscale tribological performance is required.[5] The physicochemical mechanisms leading to the reduction of friction and wear by OFMs have been debated for almost a century. Much of the uncertainty regarding the action of OFMs originates from the fact that the films they form are extremely thin ($\approx$ 2 nm) and fragile when extracted from the liquid phase.[4] Hardy and Doubleday[6] showed that carboxylic acids produced a progressively lower friction on steel surfaces as their chain length (C_4–C_{12}). From this result, they postulated that the reduction in friction was due to the formation of vertically-oriented surfactant monolayers on the sliding surfaces.[6] Bowden and Leben[7] compared the friction of steel surfaces lubricated by the stearic acid (C_{18}) films formed by the Langmuir-Blodgett method[8] and the same carboxylic acid dissolved in a nonpolar base oil. They showed that a single monolayer of stearic acid was initially able to reduce friction down to the same level as that produced by the steel surfaces immersed in stearic acid dissolved in the base oil.[7] Their close-packed monolayer film formed from solution would today be referred to as a self-assembled monolayer (SAM).[9] Several macroscale tribometer studies have shown that, as OFM concentration in a nonpolar base oil is increased, friction decreases before reaching a constant minimum value.[10–12] This minimum friction is generally attributed to the formation of a close-packed monolayer, with near complete surface coverage.[4] However, in a recent study, Jaishankar et al.[13] suggested that minimum friction occurs at much lower OFM surface coverage than required for a close-packed monolayer.

In situ atomic force microscopy (AFM) can simultaneously probe the structure and friction of thin films at solid-liquid interfaces.[1,14] Indeed, AFM experiments have been used to study the film structure[15–17] and friction[18,19] of the SAMs formed by a range of OFMs on solid surfaces from base oil solution.

Recently, two experimental studies have given important insights on the relation between OFM surface coverage and friction. Using the quartz crystal microbalance (QCM) and

spectroscopic ellipsometry, Fry et al.[20] showed that OFMs that form monolayers with lower surface coverage gave higher friction in macroscale tribometer experiments. The same trend has frequently been observed at the nanoscale for a wide range of SAMs using AFM tips with a relatively large radius of curvature, $r_{\mathrm{tip}} \approx 50$ nm.[21–29] Similar friction-coverage behaviour was also observed at the microscale for aromatic thiol SAMs on silver surfaces with the surface force apparatus (SFA).[30] However, recent AFM experiments by Nalam et al.,[19] who used much sharper AFM tips ($r_{\mathrm{tip}} \approx 15$ nm), showed the opposite trend, *i.e.* the friction coefficient increased with increasing OFM surface coverage.

Nonequilibrium molecular dynamics (NEMD) simulations can also provide atomic-level insights into the structure and friction behaviour of OFM films inside tribological contacts.[31] For example, NEMD simulations have been used to study a range of OFMs (carboxylic acids, amides, esters) with C_{18} tailgroups adsorbed on atomically-smooth α-Fe_2O_3 surfaces[32,33] and α-Fe with nanoscale roughness features.[34,35] In these studies, OFM monolayers with high surface coverage ($\Gamma \approx 4$ nm^{-2}) showed generally lower friction than those with low surface coverage ($\Gamma \approx 1$ nm^{-2}).[33] This observation rationalised the higher friction observed in macroscale tribometer experiments for OFMs with *Z*-unsaturated tailgroups (*e.g.* oleic acid) compared to those with saturated tailgroups (*e.g.* stearic acid),[36] which form monolayers with lower surface coverage.[37]

Several NEMD simulations have also been performed to study the friction of SAMs penetrated by single nanoscale asperities. For example, Knippenberg et al.[38,39] studied friction in a close-packed ($\Gamma \approx 5$ nm^{-2}) C_{14} alkyl monolayer tethered to a diamond substrate that were indented with a spherical fullerene tip ($r_{\mathrm{tip}} = 1.3$ nm) at high sliding velocity ($v_{\mathrm{s}} = 87$ m s^{-1}). In agreement with previous experiments for octadecyltrichlorosilane (OTS) on amorphous silica (a-SiO_2) surfaces,[28] they showed that plowing of adsorbed monolayers can be a significant contribution to friction.[38] Chandross et al.[40] studied the indentation and friction of close-packed ($\Gamma = 4.0$ nm^{-2}) alkylsilane molecules (C_8-C_{18}) adsorbed on a-SiO_2 substrates with hemispherical a-SiO_2 tips ($r_{\mathrm{tip}} = 3$–30 nm) at $v_{\mathrm{s}} = 2$ m s^{-1}. They found that,

although the friction force, F_{F}, increased when the tip radius was increased due to adhesion, the friction coefficient, μ, was almost independent of the tip radius.[40] In a recent study, Summers et al.[41] also studied friction in alkylsilane molecules (C_{18}) adsorbed at different Γ (2.0-5.0 nm^{-2}) on a-SiO_2 substrates indented by hemispherical and flat a-SiO_2 AFM tips ($r_{\mathrm{tip}} = 2$ nm) at $v_{\mathrm{s}} = 10$ m s^{-1}. For the hemispherical tip, they found that μ increased with increasing Γ,[41] as observed experimentally by Nalam et al.[19] However, NEMD simulations have not been performed for the systems studied by Nalam et al.[19] *i.e.* OFM molecules adsorbed on steel surfaces indented by single nanoscale asperities. Moreover, the physical mechanisms that lead to the opposite friction-coverage trends at the macroscale[20] and the nanoscale[19] remain unclear. This is important to understand in order to facilitate the design of new OFM molecules that form monolayers with an optimal surface coverage.

In this study, we use NEMD simulations to investigate friction of stearamide ($C_{18}H_{37}NO$) OFM films adsorbed on an atomically-smooth α-Fe_2O_3 surface indented by an a-SiO_2 tip. To ensure that molecule-molecule and molecule-surface interactions are accurately represented, we utilise an all-atom force field with OFM-surface interactions optimized from density functional theory (DFT) calculations. We investigate the effects of tip radius ($r_{\mathrm{tip}} = 4$ nm and 12 nm), sliding velocity ($v_{\mathrm{s}} = 2$–50 m s^{-1}), and surface coverage ($\Gamma = 2$–5 nm^{-2}) on the nanoscale structure and friction of the amide monolayers. Our results clarify the physical mechanisms leading to the increase in friction with increasing surface coverage observed experimentally by Nalam et al.[19] using a sharp AFM tip. Sharp AFM tips penetrate into the stiff high coverage monolayers, which show greater resistance to sliding than low coverage monolayers. We also show that, due to mechanical instabilities during sliding, friction originates at the leading edge of the tip, while thermal dissipation occurs at the trailing edge.

Materials and Methods

Simulation setup

The simulation setup for two example systems, with different tip radii, are shown in Fig. 1a ($r_{\mathrm{tip}} = 4$ nm) and Fig. 1b ($r_{\mathrm{tip}} = 12$ nm). The systems consist of a-SiO_2 tips above atomically-smooth hematite (α-Fe_2O_3) substrates that are covered by amide OFM monolayers. The setup is similar to that used by Nalam et al.[19] for their AFM experiments. Most of the tips used in AFM experiments are made from Si or Si_3N_4,[40] which will quickly oxidise when exposed to air to form an outer SiO_2 layer.[42] In AFM experiments, Si-based tip radii are generally of the order of tens of nanometers.[40] The range of a-SiO_2 tip sizes in the current simulations ($r_{\mathrm{tip}} = 4$–12 nm) are similar to those employed in previous experimental[19] and NEMD studies.[40,41] A hemicylindrical tip shape is employed, which is periodic in the y-direction.[43] Compared to a hemispherical tips, hemicylindrical tips decouple the required system size in the y-direction from the other directions, which can dramatically reduce the computational expense for large tip radii.[44] The α-Fe_2O_3 substrate is used as a model for steel surfaces, which form outer oxide layers when exposed to air.[45] The α-$Fe_2O_3(0001)$ surface is chosen because of its high thermodynamic stability.[46] The substrate is periodic in the x and y directions and has dimensions of: $\mathrm{L}_x = 20.2$ nm, $\mathrm{L}_y = 2.8$ nm, and $\mathrm{L}_z = 1.5$ nm. 10 nm of space was added above the substrate in the z-direction.

We selected stearamide ($C_{18}H_{37}NO$), a surfactant with an amide headgroup and a saturated linear C_{18} tailgroup, as a model OFM.[4] In addition to their use as OFM additives in engine lubricants for steel surfaces, fatty amides are also used to control friction in automatic transmission fluids,[48] and for polymer processing.[49,50] Since adsorption from solution is very slow on MD timescales, stearamide molecules were placed close to the surface at different coverages.[33] This approach yields preformed monolayers, similar to those formed experimentally using the Langmuir-Blodgett method.[8] Four different coverages ($\Gamma = 2$–5 nm^{-2}) were considered, with stearamide molecules randomly distributed on the α-$Fe_2O_3(0001)$ substrate,

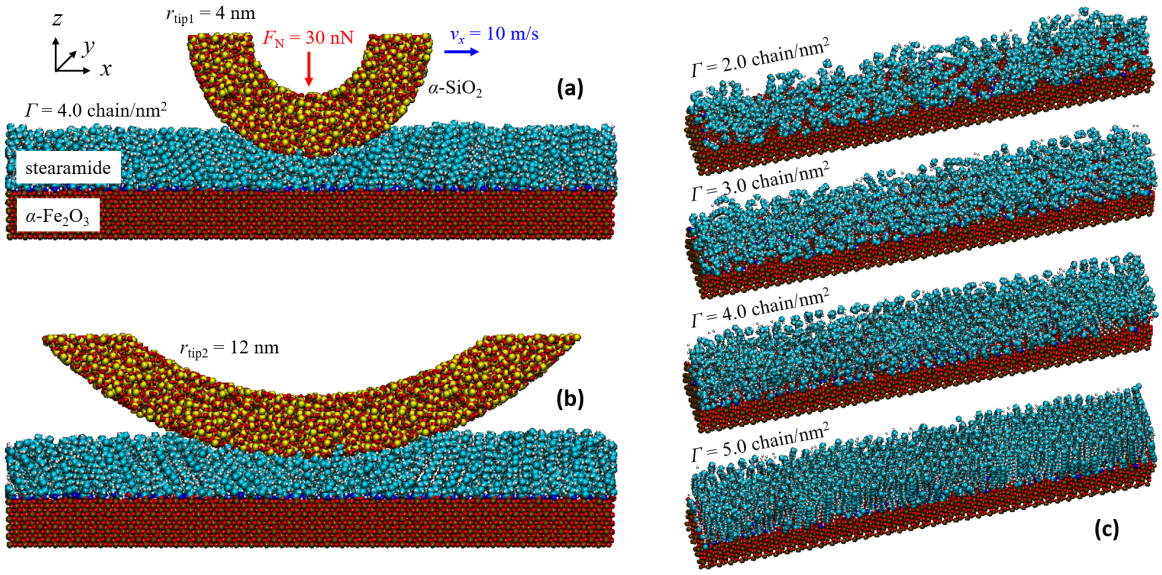

Figure 1: Snapshots of representative systems of stearamide monolayers ($\Gamma = 4$ nm^{-2}) on α-Fe_2O_3 substrates ($x = 20.2$ nm, $y = 2.8$ nm, and $z = 1.5$ nm) indented by a-SiO_2 tips, with $r_{tip} = 4$ nm (a) and 12 nm (b). Snapshots of stearamide monolayers with surface coverage (c), $\Gamma = 2$–5 nm^{-2} on α-Fe_2O_3 (tips not shown). Rendered with VMD:[47] Fe atoms are shown in brown, O in red, N in blue, C in cyan, H in white, and Si in yellow.

as shown in Fig. 1c. These are the same coverage values that were considered by Summers et al.[41] in their NEMD simulations of OTS monolayers on a-SiO_2 surfaces. Rather than the surface coverage, the concentration of OFM in base oil is typically varied in macroscale tribometer experiments,[36] since this is much easier to measure and control. However, depletion isotherm, polarised neutron reflectometry (PNR),[37,51] and QCM experiments[13,19,20,52] can be used to measure the surface coverage at a given OFM concentration. Adsorption experiments have not been performed for stearamide on iron oxide surfaces; however, those for stearic acid suggested a maximum $\Gamma \approx 4$ nm^{-2} on iron oxide from n-dodecane.[37] The highest coverage considered in this study (5 nm^{-2}) has been achieved for stearic acid on iron surfaces[53] using the Langmuir-Blodgett technique.[8]

To minimise the computational expense, only the polar OFM molecules, not the nonpolar base oil molecules, are considered in this study. This choice is not expected to significantly affect the friction results for the range of surface coverages, tip radii, and loads studied here. Previous AFM experiments[28] and NEMD simulations[38] have shown that, in the chosen parameter space, friction is dominated by the tip plowing through the adsorbed monolayers. For surfaces coverages lower than those studied here $\Gamma < 2$ nm^{-2} the absence of base oil molecules would be expected to have a non-negligible effect on friction, since the OFM molecules may not completely cover the surface, even when orientated parallel to the surface.

Force field

The stearamide molecules are represented with the long chain-optimized potential for liquid simulations-all atom (L-OPLS-AA) force field.[54,55] This force field has been shown to accurately describe the structure and friction behaviour of OFM monolayers adsorbed on iron oxide surfaces.[56] The bonded and nonbonded parameters of the stearamide molecule can be found in Jorgensen et al.[54] (N, O) and Siu et al.[55] (C, H).

In the α-Fe_2O_3 substrate, harmonic bonds with a force constant of 130 kcal mol^{-1} Å^{-1} were added between atoms within 0.3 nm of each other in their lattice positions. The bond

lengths were based on the interatomic distances reported by Blake et al.[57] from diffraction experiments. This has been shown in previous simulations to provide both realistic mechanical properties and efficient thermal dissipation.[58] DFT calculations of hexanamide adsorption on α-Fe_2O_3(0001) have shown strong chemisorption interactions to occur between amide headgroups and the surface atoms.[46] For the force field used in this study, the molecule-surface parameters were optimised to match DFT adsorption energies for a wide range of conformations of amides on α-Fe_2O_3(0001).[59] Morse and Coulomb potentials were used for the strong headgroup-surface interactions (O_{amide}-Fe_{surf}, N_{amide}-Fe_{surf}, H_{amide}-O_{surf}), while Lennard-Jones and Coulomb potentials were used for the weaker tailgroup-surface interactions.[59] The headgroup-surface Morse parameters, as well as Fe and O Lennard-Jones and partial charge parameters, are given in Ayestarán Latorre et al.[59]

The a-SiO_2 tip was prepared by annealing β-cristobalite using a modified van Beest-Kramer-van Santen potential.[60] The β-cristobalite cell was heated to 4,000 K and quenched to 300 K at a cooling rate of 2.5 K ps^{-1}, which yielded a-SiO_2 with a density of 2.2 g cm^{-3}. The full procedure for the annealing is described in Döpke et al.[61] From this system, hemicylinders were cleaved, which were then energy minimised using the same potential. During the indentation and sliding simulations, the tips were treated as rigid bodies, as significant deformation is not expected due to the much higher stiffness of silica compared to the monolayers.[41] The Si and O Lennard-Jones and partial charge parameters for atoms in the tips, which control the tip-amide and tip-substrate interactions, were taken from Summers et al.[41]

Geometric mean mixing rules were used for Lennard-Jones interactions between unlike atoms.[54] The Lennard-Jones and Morse interactions were cut off at a distance of 1.2 nm.[59] A slab implementation of the particle-particle, particle-mesh algorithm[62] with a relative force accuracy of 10^{-5} was used for the Coulombic interactions.

Simulation procedure

NEMD simulations were performed using the large-scale atomic/molecular massively parallel simulator (LAMMPS) software.[63] The velocity Verlet integration algorithm was used with a time step of 1 fs. All systems were energy minimised before they were equilibrated at a temperature of 300 K for 1 ns. The positions of the bottom layer of atoms (0 nm $< z <$ 0.1 nm) in the α-Fe_2O_3(0001) substrate were fixed. Temperature was controlled with a Langevin thermostat with a coupling time of 0.1 ps.[64] The thermostat was applied to the middle layer (0.1 nm $< z <$ 1.0 nm) of substrate atoms and was coupled to the thermal velocities in the y-direction, *i.e.* perpendicular to both compression and sliding. Several previous studies have demonstrated the importance of thermostatting the substrate rather than the fluid molecules during confined NEMD simulations.[65–67]

After the system was equilibrated, a constant normal force (1–30 nN) was added to the tip in the z-direction to compress the stearamide monolayer. Similar loads have been used in previous experiments[19] and NEMD simulations[38,40,41] of monolayers indentation by nanoscale asperities. These forces lead to estimated mean Hertz pressures, P_{mean} = 0.04–2 GPa for the tip sizes considered (r_{tip} = 4–12 nm). These P values are directly relevant to AFM experiments of OFM films[19] as well as the operation of OFMs under boundary lubrication conditions.[4] Compression simulations were performed for approximately 1 ns, which was the time taken for the tip-surface distance and average normal force on the tip to reach a steady state.

Next, the tip was moved at a constant sliding velocity, v_{s}, in the x-direction while maintaining the applied normal force. In most NEMD simulations of the current study, v_{s} = 10 m s^{-1}, but other values (v_{s} = 2–50 m s^{-1}) were also considered in a subset of simulations. The NEMD velocities[38,40,41] are several orders of magnitude higher than those reached in AFM experiments ($\mathcal{O}$ μm s^{-1})[24,25,28,29] or macroscale tribometer experiments ($\mathcal{O}$ mm s^{-1}).[20,36] The sliding velocities are, however, quite similar ($\mathcal{O}$ m s^{-1}) to those which are experienced by components in applications such as micro-electromechanical systems (MEMS)[68] and in-

ternal combustion engines.[69] Previous studies of similar systems have shown that friction coefficients obtained from NEMD simulations can agree well with extrapolations from experiments conducted at lower sliding velocities.[56] The normal and friction forces represent the total forces on the sliding tip in the z and x directions respectively. The sliding simulations were performed for a sufficiently large sliding distance (50 nm) to ensure that a nonequilibrium steady state was obtained for all sliding velocities.[70] The normal and friction forces presented in the Results and Discussion section were averaged over the final 30 nm of sliding. In contrast to previous NEMD simulations with flat substrates,[71] we did not find that friction depended much on the relative orientation of the tip to the collective molecular tilt of the OFM molecules.

Results and Discussion

Indentation Depth

Previous AFM experiments[27,28] and NEMD simulations[38,41] have suggested that the friction in various SAM films indented by sharp asperities is dominated by molecular plowing. To help understand the nature of the frictional dissipation within the OFM monolayers investigated here, we first investigated the indentation depth of the tip during sliding for the different systems and conditions considered. We found that all of the amide headgroups remain attached to the surface under even the most extreme pressure and sliding conditions studied. This is due to the strong chemisorption interactions between the amide headgroup and surface atoms,[59] which is consistent with DFT calculations[46] and X-ray photoelectron spectroscopy experiments.[51]

Fig. 2 shows how the monolayer film thickness, h, varies along the sliding direction ($+x$), with a lateral resolution of 0.5 nm for $r_{\mathrm{tip}} = 4$ nm (a) and 12 nm (b). Here, h is defined as the distance between the centre of the topmost substrate atoms and the topmost stearamide atoms in the z-direction. The x-coordinates in Fig. 2 are relative to the centre of the tip.

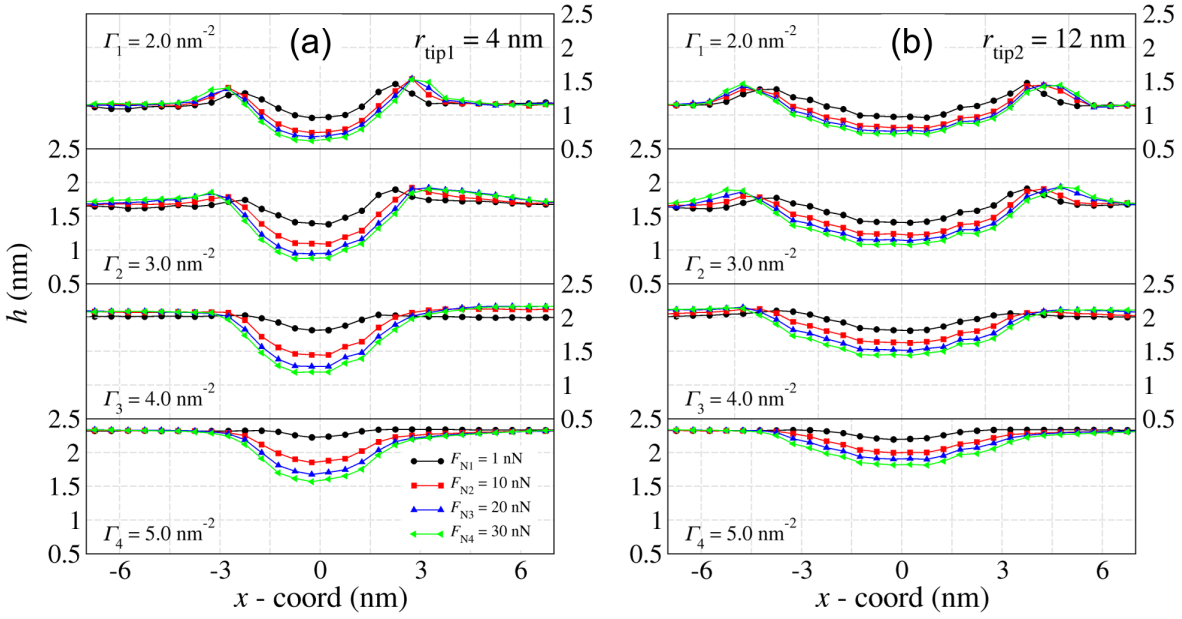

Figure 2: Film thickness, h, profiles in the sliding direction ($+x$) for tip radius, $r_{\text{tip}} = 4$ nm (a) and $r_{\text{tip}} = 12$ nm (b). Coordinates are relative to the tip centre. Standard deviations are smaller than the symbol size.

In Fig. 2, a reduction in film thickness is observed underneath the tip centre in all cases, indicating that the stearamide monolayers are penetrated by the tip during sliding. This suggests that thickness is reduced either due to viscoelastic deformation[72] or plowing[28,38] of the monolayers by the tip. Note that, unlike the plastic deformation during the plowing of solids,[73] only elastic deformations occur during molecular plowing. The average monolayer film thickness in the z-direction can be determined from the height of the monolayer in the undisturbed region of the film thickness profiles, away from the tip centre. The lateral dimensions are sufficiently large such that, in the undisturbed region, h is the same as in the absence of the tip within statistical uncertainty. In the undisturbed region, h increases with increasing coverage, from 1.2 nm at $\Gamma = 2$ nm^{-2} to 2.3 nm at $\Gamma = 5$ nm^{-2}. The film thickness values are within 5 % of those obtained in previous NEMD simulations of OTS (also linear, C_{18} tailgroup) monolayers at the same surface coverages on a-SiO_2.[41] This range of thicknesses is also consistent with that obtained from adsorption experiments for different

OFMs on a-SiO_2 (0.5–2.2 nm)[20] and α-Fe_2O_3 (2.2 nm)[37] surfaces. The film thicknesses imply that, at high coverage ($\Gamma = 5$ nm^{-2}), the molecules away from the tip are orientated perpendicular to the surface, while at low coverage ($\Gamma = 2$ nm^{-2}), they are at approximately 45°. The film thicknesses are towards the lower end of the experimental range estimated by Nalam et al.[19] (0.5–0.7 nm) for their amine OFMs on steel surfaces. This comparison suggests that only relatively low surface coverages were obtained for all of the bulky OFM molecules studied by Nalam et al.[19]

The film thickness profiles in Fig. 2 are mostly symmetrical, with tailgroups underneath the tip being compressed and displaced towards both the leading and trailing edges of the tip. As expected, the sharper tip (Fig. 2a) shows deeper, more localised penetration than the blunter tip (Fig. 2b). An increase in h compared to the undisturbed region at the leading and trailing edge of the tip is observed at low coverage ($\Gamma = 2$–3 nm^{-2}). Unlike for the indentation of crystalline solids,[74] tailgroup atoms are not pushed upwards in front of the tip, since they are pulled back towards the headgroups that remain anchored to the substrate. At high coverage ($\Gamma = 5$ nm^{-2}), there is a small reduction in h at the leading edge of the tip. This is due to the closely-packed molecules being pulled downwards to accommodate tip motion over neighbouring molecules, even before they themselves come into direct contact with the tip.

Even for the lowest coverage ($\Gamma = 2$ nm^{-2}), smallest tip ($r_{\mathrm{tip}} = 4$ nm), and largest load ($F_{\mathrm{N}} = 30$ nN) considered, the tip and the substrate remain separated at a distance of approximately 0.5 nm. This observation suggests that the OFM films can prevent direct solid-solid contact under very high pressures (> 2 GPa), even at relatively low surface coverage.[13] Similarly, previous AFM experiments of close-packed hexadecanethiol monolayers on the Au(111) surface suggested that they were durable up to an average pressure of 3.7 GPa.[75]

Fig. 3 shows the change in tip-monolayer indentation depth, d_p, with surface coverage, Γ, for the different loads, F_{N}, considered. Here, d_p is defined as the difference between the

z-positions of the bottom of the tip and the top of the undisturbed amide monolayer. For all of the systems studied, d_p increases with increasing load. At the lowest load considered (1 nN), the indentation depth is < 0.3 nm, which is equivalent to the length of two extended C–C bonds. As the load increases, d_p increases to a maximum value of around 1 nm, which is roughly equal to half of the length of the OFM molecule.

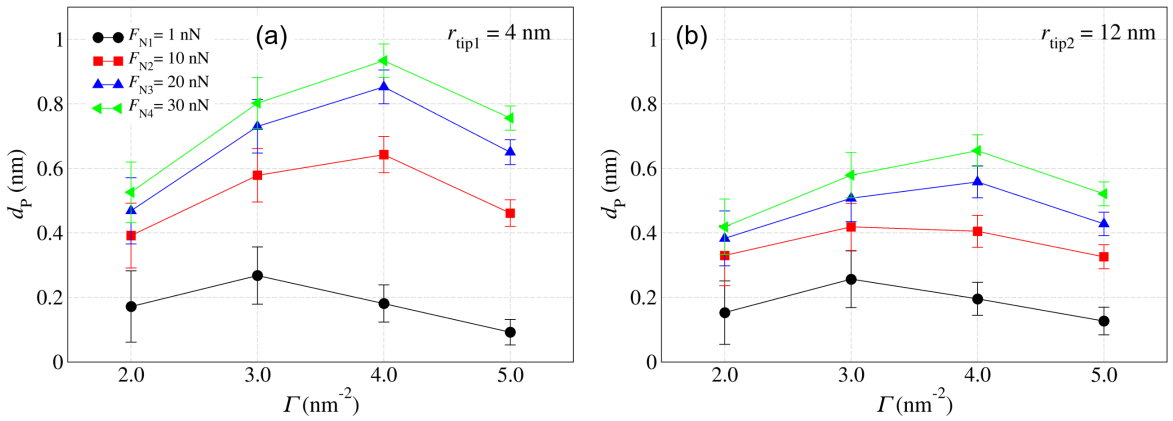

Figure 3: Change in tip-monolayer indentation depth, d_p, with surface coverage, Γ, for the different loads, F_N, considered with $r_{tip} = 4$ nm (a) and $r_{tip} = 12$ nm (b). Vertical bars represent the standard deviations from the running averages measured during the final 30 nm of sliding.

A deeper indentation is revealed for $r_{tip} = 4$ nm (Fig. 3a) compared to $r_{tip} = 12$ nm (Fig. 3b), which is due to the reduced contact area and thus higher pressure. For both tip sizes, d_p increases markedly with load between $F_N = 1$–10 nN, to a lesser degree between 10–20 nN, and remains almost constant between 20–30 nN. This suggests that collective molecular tilt and molecular defects[76] can accommodate the indentation of the tip only up to a certain point, beyond which the monolayers become much less compressible. Previous MD simulations by Gao et al.[77] have shown that nonpolar hydrocarbons also become much less compressible when they are confined to distances < 1 nm. Although the reduction in compressibility occurs at a similar tip-substrate distance (< 1 nm) to nonpolar hydrocarbons at low coverage, it occurs at much larger distances at high coverage (> 1.5 nm). This observation suggests that the lower compressibility of high coverage films at high loads is

not purely attributable to confinement effects.

In Fig. 3, d_p has a non-monotonic dependence on surface coverage, with the maximum indentation depth occurring at intermediate coverage (usually $\Gamma = 4$ nm^{-2}). This suggests that the elastic modulus of the films decreases between $\Gamma = 2$–4 nm^{-2} and then increases between $\Gamma = 4$–5 nm^{-2}. As Γ is increased, there are two competing effects which determine the elastic moduli of the monolayers; (i) decreasing confinement[77] and (ii) increasing molecular packing density.[28] Our results suggest that between $\Gamma = 2$–4 nm^{-2}, the decrease in elastic modulus due to (i) outweighs the increase due to (ii), while the opposite is true between $\Gamma = 4$–5 nm^{-2}. This implies that a solid-like SAM, with high elastic modulus, is formed when the coverage reaches 5 nm^{-2},[41] even in the absence of confinement effects. For the lowest loads considered (1 nN), the transition from increasing to decreasing indentation depth with increasing coverage occurs at lower coverage ($\Gamma = 3$–4 nm^{-2} than at higher loads (4–5 nm^{-2}). This is because, at 1 nN, the tip-substrate separation distance is always $<$ 1 nm (Fig. 2), so the elastic modulus is governed more by packing density rather than by confinement effects.

Friction

Now that we have quantified the degree of indentation for the systems and conditions studied, we can link this to the kinetic friction measured in the systems during sliding. Fig. 4 shows the change in the friction force, F_{F}, with normal force, F_{N}, for different Γ and r_{tip}.

For both tip sizes, F_{F} increases linearly with F_{N} with a finite intercept in Fig. 4. This linear trend is consistent with Amontons' first law of friction, $F_{\mathrm{F}} = \mu F_{\mathrm{N}}$, where μ is the friction coefficient. Since this expression cannot account for the non-zero intercepts observed in Fig. 4, Derjaguin[78] proposed a modification:

$$F_{\mathrm{F}} = \mu F_{\mathrm{N}} + F_0 \tag{1}$$

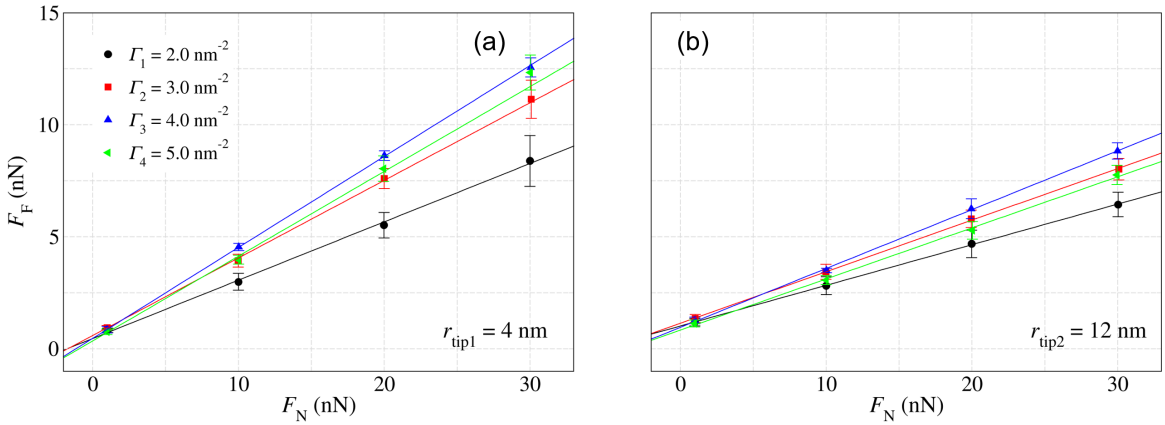

Figure 4: Change in the friction force, F_F, with normal force, F_N, for the different surface coverages, Γ, of stearamide considered (2–5 nm^{-2}) with a 4 nm (a) and 12 nm (b) tip radius, r_{tip}. Solid lines are linear fits to the data. Vertical bars represent the standard deviations from the running averages measured during the final 30 nm of sliding.

where F_0 is the so-called Derjaguin offset which is attributable to adhesive forces. This expression was used by Briscoe and Evans[79] to describe the friction between Langmuir-Blodgett[8] films of carboxylic acid OFMs (C_{14}-C_{22}) on atomically-smooth mica substrates. The expression has frequently been used to describe friction data from AFM experiments of SAMs on solid surfaces[26,80] as well as NEMD simulations of OFM monolayers on surfaces with nanoscale roughness features.[34,35] Expressions that separate the plowing contribution to the friction of SAMs indented by AFM tips have been proposed by Brukman et al.[27] and Flater et al.[28] These expressions are only required when the F_F versus F_N plot is non-linear, which is not the case for any of the systems in Fig. 4 up to the maximum load (30 nN). Therefore, we use the simpler modified form of Amontons' first law of friction due to Derjaguin[78] to describe our F_F versus F_N data, which is shown in Equation (1).

Comparing Fig. 4a and Fig. 4b, F_F is higher for the sharper 4 nm tip than for the 12 nm tip at all but the lowest normal force (1 nN). The gradients and intercepts of the linear fits in Fig. 4 were used to calculate μ and F_0, respectively, using Equation (1).[78] Fig. 5 shows the change in friction coefficient, μ (a) and Derjaguin offset, F_0 (b) with Γ for the

two different r_{tip}. It is clear from Fig. 5a that, for all of the Γ values considered, μ is higher for $r_{\text{tip}} = 4$ nm than for $r_{\text{tip}} = 12$ nm. The larger μ for the smaller tip is due to the higher pressure, which leads to deeper indentation (Fig. 3), and thus a larger plowing contribution to friction. Previous NEMD simulations by Chandross et al.[40] suggested μ was essentially independent of r_{tip} in the range 3–30 nm. This difference could originate from the fact that these previous simulations used shorter alkyl tailgroups (C_{11}) and fewer F_N values spanning a narrower range (0–20 nN) to estimate μ than the current study.

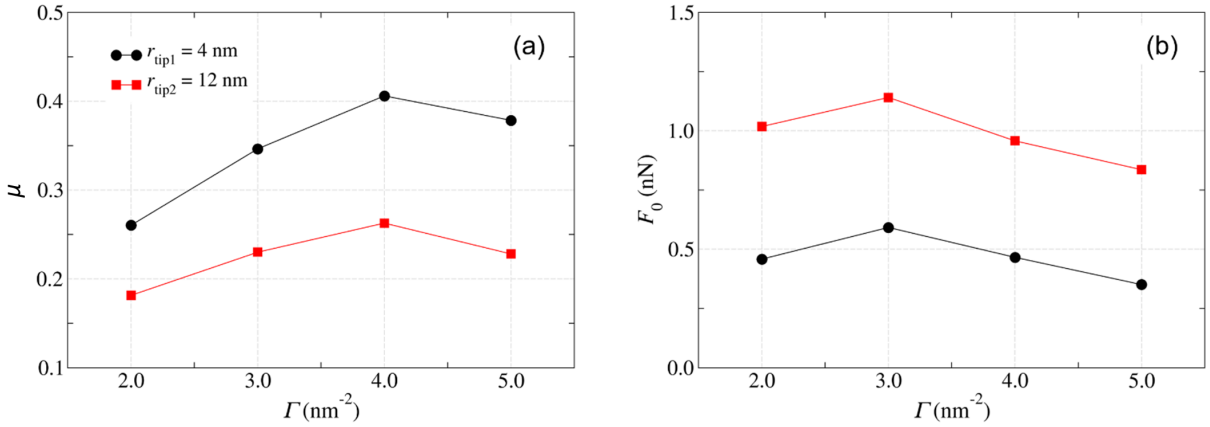

Figure 5: Change in the friction coefficient, μ, (a) and Derjaguin offset, F_0, (b) with stearamide surface coverage, Γ, for tip radii, $r_{\text{tip}} = 4$ nm (black circles) and 12 nm (red squares). Solid lines are guides for the eye.

Previous NEMD simulations of stearamide on flat α-Fe_2O_3 gave friction that decreased linearly from $\mu = 0.22$ at $\Gamma = 1.4$ nm^{-2} to $\mu = 0.16$ at $\Gamma = 4.3$ nm^{-2}.[59] The μ values in Fig. 5a with the top surface containing nanoscale curvature are larger than those obtained from previous simulations with flat surfaces.[59] The same observation was made by Knippenberg et al.[39] from NEMD simulations comparing friction from C_{14} alkyl chains grafted on a diamond surface compressed by either a spherical fullerene tip ($r_{\text{tip}} = 1.3$ nm) or a flat amorphous carbon slab. Moreover, de Beer and Müser[81] showed using NEMD that, for polymer brush-bearing surfaces, systems with nanoscale curvature ($r_{\text{tip}} = 50$ nm) provided additional dissipation mechanisms compared to those with flat surfaces. The higher friction for curved surfaces compared to flat ones is due to additional dissipation mechanisms from

the penetration of the sliding surfaces into the monolayers.

In the previous NEMD simulations with flat surfaces, the reduction in μ with increasing surface coverage was due to the formation of more solid-like monolayers, with reduced molecular interdigitation.[33,59] Several experimental AFM studies have also shown that μ decreases as Γ increases.[21–29] A reduction in μ with increasing Γ has also recently been observed in macroscale tribometer experiments by Fry et al.[20] However, Fig. 5a shows that, for sharp AFM tips, friction initially increases with coverage due deeper indentation (Fig. 3).

In Fig. 5a, μ shows a non-monotonic dependence on surface coverage for both tip sizes, with the maximum friction coefficient occurring at intermediate coverage ($\Gamma = 4$ nm^{-2}). The coverage corresponding to maximum μ is the same as the coverage at which maximum d_p is observed in Fig. 3, confirming that molecular plowing governs the frictional response.[28] Non-monotonic friction-coverage dependence has recently been observed in NEMD simulations of a single asperity sliding on a crystalline surface lubricated by an atomic fluid.[82] In these systems, the tip and substrate were incommensurate, meaning that the presence of atoms between the tip and substrate increased friction until the coverage approached the level required to form a complete monolayer.[82] Non-monotonic friction-coverage behaviour has also been observed in microscale SFA experiments Yoshizawa et al.[83] using zwitterionic surfactants with a range of headgroup and tailgroup structures on mica surfaces in aqueous environments. The non-monotonic response was attributed to a transition from liquid-like, to amorphous, and to solid-like monolayers with increasing coverage (Γ = 2–5 nm^{-2}).[83]

Despite a large number of AFM studies involving a wide range of different types of SAM,[21–29] non-monotonic friction-coverage dependence has not been observed experimentally in non-aqueous environments. Most previous AFM studies used relatively blunt tips ($r_{\text{tip}} \approx 50$ nm),[21–29] which, based on the results shown in Fig. 2 and Fig. 3, are likely to only give shallow indentation depths in the load range considered (F_{N} = 1–30 nN). Conversely, Nalam et al.[19] used much sharper AFM tips ($r_{\text{tip}} \approx 15$ nm), meaning that similar indentation depths are expected to those observed in the current simulations in Fig. 3b (r_{tip}

= 12 nm). Nalam et al.[19] found that, in contrast to the AFM experiments with larger tips, μ increased with increasing Γ for amine OFM monolayers on steel surfaces. Using NEMD simulations, Summers et al.[41] also showed that μ increased with increasing Γ for OTS SAMs indented by a very sharp AFM tip ($r_{\mathrm{tip}} = 3$ nm). The same trend is observed between low and intermediate coverage ($\Gamma = 2$–4 nm^{-2}) in Fig. 5a. A decrease in μ between intermediate and high coverage ($\Gamma = 4$–5 nm^{-2}) was also observed, which was not seen in the experiments by Nalam et al.[19] or the NEMD simulations by Summers et al.[41] Previous depletion isotherm and PNR experiments[37] suggest that the OFMs used by Nalam et al.,[19] which contained a mixture of saturated and Z-unsaturated tailgroups, were unlikely to have reached the highest coverage considered in the current study ($\Gamma = 5$ nm^{-2}). Indeed, Nalam et al.[19] estimated that the OFMs they used only reached surface coverages of ≈ 2 nm^{-2} using QCM. In future studies, we expect that non-monotonic friction-coverage behaviour will be observed experimentally by using a combination of sharp AFM tips and surfactants known to form close-packed monolayers (*e.g.* stearic acid[37]).

Fig. 5b shows that adhesion, as quantified by F_0 (Equation (1)),[78] is larger for the blunter tip, as expected due to the increased tip-monolayer contact area.[40] At very low load ($F_{\mathrm{N}} = 1$ nN), F_0 can contribute more than 50 % of the overall F_{F} in Fig. 5b. However, at higher loads, which are more application-relevant, F_0 becomes much less important, for example $F_0 < 10$ % of F_{F} at 20 nN. In previous NEMD simulations of OFM monolayers with fully-periodic surfaces containing nanoscale roughness features, F_0 only significantly enhanced friction at low surface coverage.[34,35] In Fig. 5b, there is also a general decrease in F_0 with increasing surface coverage for the single-asperity systems studied here. Looking at Fig. 2, this decrease in F_0 can be attributed to the general reduction in tip-monolayer contact area as surface coverage increases.

Fig. 6 shows the change in F_{F} with v_{s} for different surface coverages ($\Gamma = 2$–4 nm^{-2}) and tip sizes ($r_{\mathrm{tip}} = 4$–12 nm). Although v_{s} is several orders of magnitude higher in the NEMD simulations compared to the AFM experiments, the thermostatting procedure adopted en-

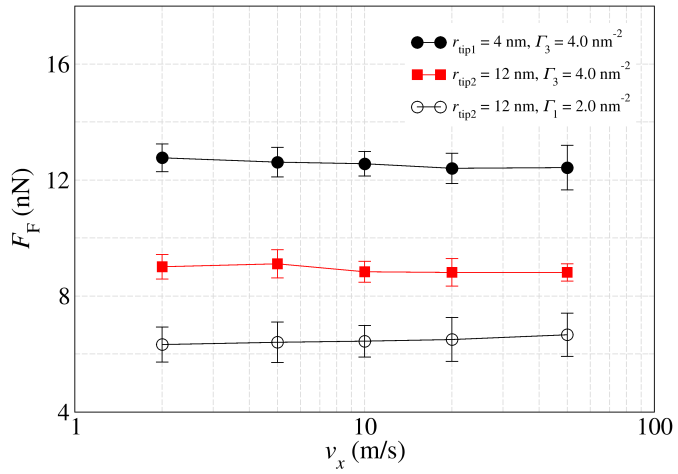

Figure 6: Change in the mean friction force, F_{F}, with sliding velocity v_{s} for different surface coverages (Γ = 2–4 nm^{-2}) and tip radii (r_{tip} = 4–12 nm). Solid lines are guides for the eye. Vertical bars represent the standard deviations from the running averages measured during the final 30 nm of sliding.

sures that the friction-induced temperature rise is negligible at the iron oxide surface.[64] Therefore, the friction results from the NEMD simulations are expected to be in agreement with extrapolations from experiments conducted at lower sliding velocities, as shown previously for OFM-lubricated systems.[33,56] Fig. 6 shows that F_{F} is insensitive to sliding velocity in the range studied (v_{s} = 2–50 m s^{-1}), which is consistent with AFM experiments that used sharp tips.[19]

In order for sliding velocity-independent (*i.e.* Coulomb) friction to be obtained in a single-asperity contact, elastic or plastic instabilities must occur during sliding,[84] as rationalized in the Prandtl model.[85] The Prandtl model consists of a single, thermalized atom attached to a spring, which is dragged over a sinusoidal potential representing the surface energy corrugation of a counterface. During an instability, the stable position of an atom suddenly disappears as it quickly moves downward to the next minimum. In this process, potential energy is lost, the amount of which depends in leading order on the sliding distance rather than on the sliding velocity. Such a process implies hysteresis, since the atom would not

quickly revert to its previous metastable site if the sliding direction were instantaneously reversed.[84] While Prandtl envisioned primarily non-linear elastic hysteresis in models of isolated atoms,[85] the concept of instabilities leading to Coulomb-type friction extends to many different processes. In fact, Prandtl rightfully claimed that his model can be used to describe the transition from Stokes to Coulomb friction,[84] as well as the shear thinning of liquids.[86] The model is now most commonly applied to interpret AFM friction data for tips sliding directly on solid surfaces.[87] In the remainder of this study, we investigate the mechanical instabilities in the OFM monolayers by investigating the spatial distribution of normal and friction forces, the molecular morphology, and thermal dissipation.

Fig. 7 shows the spatial distribution of the tip-monolayer shear stress, σ_{zx}, and normal stress (pressure), σ_{zz}, for both tip radii at the highest load considered (F_{N} = 30 nN). The local stresses are calculated by dividing the sum of the tip-monolayer forces in each bin (Δx = 0.2 nm) by its area in the xy plane. The total stresses can be obtained by integrating over the area under these curves.[38] For σ_{zx}, positive values resist tip motion, while negative values assist tip motion. The x-coordinates in Fig. 7 are relative to the tip centre and the sliding direction is $+x$.

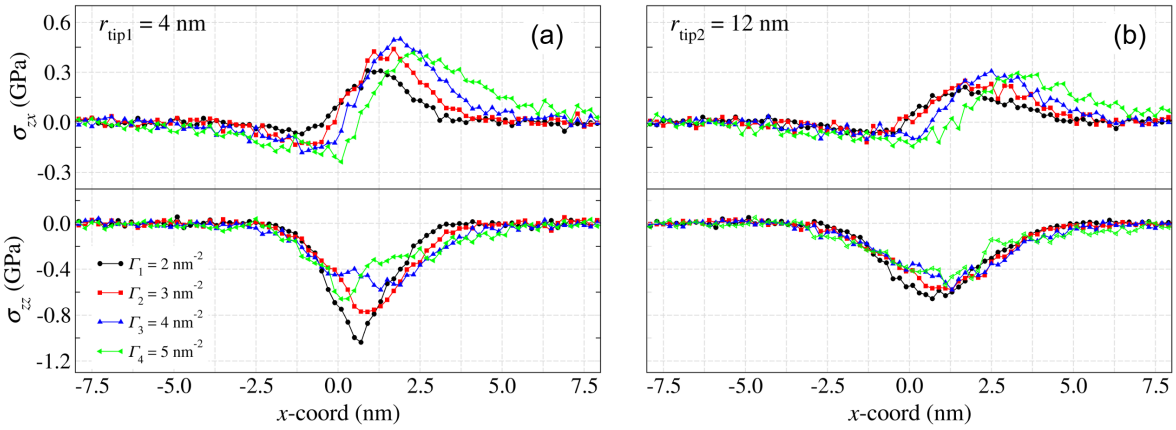

Figure 7: Spatial distribution of shear stress, σ_{zx}, and normal stress, σ_{zz}, for tip radii, r_{tip} = 4 nm (a) and 12 nm (b), at the highest load considered (F_{N} = 30 nN). Sliding direction is $+x$. Standard deviations are smaller than the symbol size.

Fig. 7 shows that, in general, σ_{zx} is localised in OFM atoms close to the leading edge of the tip, with the positive sign indicating that these atoms resist tip motion. This observation is consistent with previous NEMD simulations of a simple tip-on-flat model system lubricated by an atomic fluid[88] as well as close-packed alkyl monolayers ($\Gamma = 4.6$ nm^{-2}) indented with a spherical fullerene tip ($r_{\mathrm{tip}} = 1.3$ nm) at high sliding velocity ($v_{\mathrm{s}} = 87$ m s^{-1}).[38,39] Fig. 7 indicates that this localisation of friction is also clear for non-tethered OFM molecules at lower coverages ($\Gamma = 2$–4 nm^{-2}) and sliding velocities ($v_{\mathrm{s}} = 10$ m s^{-1}). Another observation from Fig. 7 is that atoms located close to the trailing edge assist tip motion (negative σ_{zx}), particularly at high coverage ($\Gamma = 4$–5 nm^{-2}).

For the sharper tip (Fig. 7a), the σ_{zx} peaks are larger and more strongly localised than for the blunter tip (Fig. 7b). In Fig. 7a, σ_{zx} decays to zero within 3 nm of the centre of the tip at low coverage ($\Gamma = 2$ nm^{-2}), while it extends to over 8 nm at high coverage ($\Gamma = 5$ nm^{-2}). This suggests that molecular deformation extends much further in front of the leading edge of the tip at high coverage, suggesting slower relaxation as a result of the higher molecular density.

The peak σ_{zx} is lowest for $\Gamma = 2$ nm^{-2} and remains similar between 3–5 nm^{-2}. Looking at Fig. 5a, μ was also lowest for $\Gamma = 2$ nm^{-2}, similar for 3 nm^{-2} and 5 nm^{-2}, and highest for 4 nm^{-2}. The increase in μ between $\Gamma = 2$–4 nm^{-2} can therefore be attributed to the larger peak σ_{zx}, as well as a broader distribution of σ_{zx} in the sliding direction. The reduction in μ between $\Gamma = 4$–5 nm^{-2} is due to lower peak σ_{zx}, as well as negative σ_{zx} at the trailing edge, which indicates pushing forces on the tip from these molecules. Thus, while the resistance to sliding from the leading edge of the tip is comparable for $\Gamma = 4$ nm^{-2} and $\Gamma = 5$ nm^{-2}, the pushing force from the trailing edge is greater for the latter, leading to lower overall friction.

For the large tip ($r_{\mathrm{tip}} = 12$ nm), the shape of the distribution of σ_{zz} is quasi-parabolic, as assumed in continuum contact mechanics models (*e.g.* Hertz). However, for the smaller tip ($r_{\mathrm{tip}} = 4$ nm), the σ_{zz} distribution is sharper and more strongly localised, indicating higher peak pressures than would be predicted using continuum models. Similar behaviour has

previously been observed in MD simulations of contacting solid nanoasperities[43] as well as amorphous silica nanoasperities partially separated by low coverage OTS monolayers.[89] For both tip sizes, the maximum σ_{zz} is not localised directly underneath the center of the sliding tip, but rather towards the leading edge. This implies that the peak pressure is experienced by molecules just in front, rather than directly underneath the sliding tip. Similar observations have been made from previous NEMD simulations of close-packed alkyl monolayers indented with a spherical fullerene tip.[38,39]

In simple model systems lubricated by atomic fluids,[88] it was also found that friction forces were localised at the leading edge of the tip; however, no pushing forces were observed at the trailing edge. Likewise, various systems show dissipation to take place at other locations than where friction forces are transmitted between two solids. For example, when intergranular sliding within a body is induced by a tribological interface, a significant amount of energy can be dissipated at those grain boundaries.[90] Similarly, rubber friction is thought to be caused to a significant degree by bulk viscoelastic deformation.[91] In our case, the dissipation takes place near the interface, but not directly in the region where the friction forces act.

Morphology and Dissipation

To explore connections between the monolayer morphology and friction, we also investigated changes in molecular orientation and thermal dissipation during sliding. This should also help to rationalise the insensitivity of monolayer friction to sliding velocity. For this purpose, the mean positions of coarsened tailgroup carbon atoms projected in the xz plane ($\boldsymbol{r}_{\mathrm{mean}}$) and their tensor of gyration ($R_{\alpha\beta}$) were calculated. Fig. 8 shows a representative case where $r_{\mathrm{tip}} = 4$ nm and $F_{\mathrm{N}} = 30$ nN.

Each blue circle in Fig. 8 represents the spatially-resolved position of the i^{th} tailgroup carbon in a coarse-grained molecule j over the observation time τ_{obs}. The bin size, Δx, varies depending on Γ such that each coarse-grained molecule represents a projection of

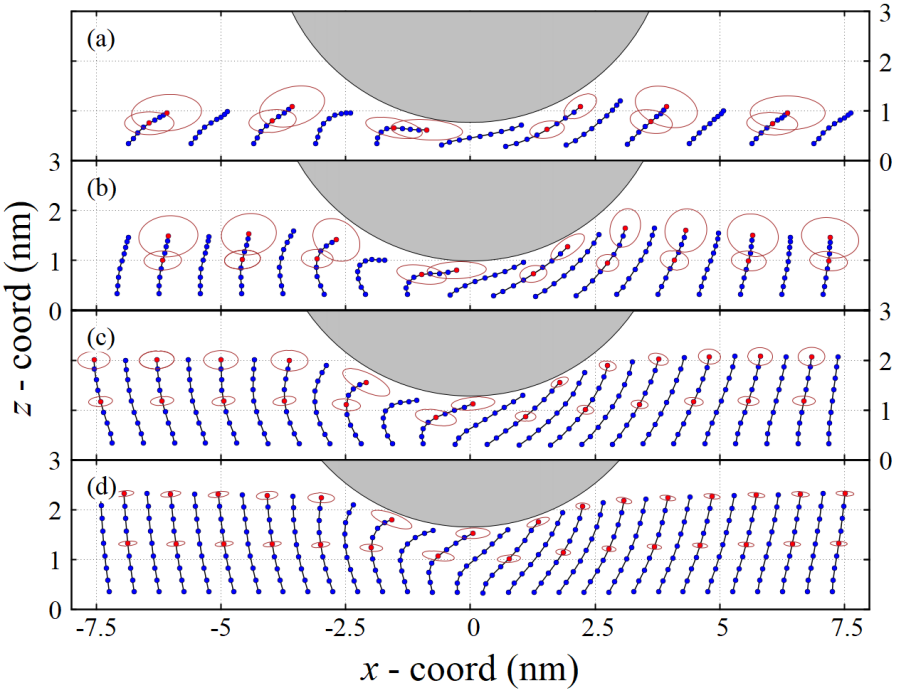

Figure 8: Coarse-grained molecular morphology of the OFM monolayers during sliding in the case of $r_{\mathrm{tip}} = 4$ nm, $F_{\mathrm{N}} = 30$ nN. Blue circles represent the mean positions of the tailgroup carbons projected in the xz plane and ellipses represent the tensor of gyration, $R_{\alpha\beta}$, of the central and terminal (in red) tailgroup atoms. To enable clearer visualization, only $\boldsymbol{r}_{\mathrm{mean}}$ with carbon index of $i = 2n$ are shown and for the same reason, R_{xz} is also shown selectively. Bin size, $\Delta x =$ (a) 1.25 nm ($\Gamma = 2$ nm^{-2}), (b) 0.833 nm (3 nm^{-2}), (c) 0.625 nm (4 nm^{-2}), and (d) 0.5 nm (5 nm^{-2}). Sliding direction is $+x$.

the average conformation of the stearamide tailgroups in the xz plane. For this purpose, Δx = 1.25, 0.833, 0.625, and 0.5 nm for Γ = 2, 3, 4, and 5 nm^{-2}, respectively. The molecule index is determined only by the coordination of carbon i=1 (the anchoring site), while the rest of the carbons are automatically associated with the same bin. Since there is only one coarse-grained molecule in each bin, the bin index is equal to the coarse-grained molecule index. The tensor of gyration of each coarse-grained segment is calculated using $(R^n_{\alpha\beta})^2 = \frac{1}{N_n}\sum_{n=1}^{N_n}\frac{1}{N_i}\sum_{i=1}^{N_i} < \delta\boldsymbol{r}^{n,i}_{\alpha}\ \delta\boldsymbol{r}^{n,i}_{\beta} >$, where α and β are Cartesian coordinates (x and z), i is the index for the carbon atoms in a coarse-grained segment (i = 1,...,N_i), n is the index for a segment in a molecular bin (n = 1,...,N_n), N_n is the number of segments in a molecular bin, $\delta\boldsymbol{r}^{n,i}_{\alpha}$ and $\delta\boldsymbol{r}^{n,i}_{\beta}$ are the change in coordinates relative to the centre of mass of the segment, and angled brackets denote an ensemble average. The red ellipses in Fig. 8 show $R_{\alpha\beta}$ for the corresponding $\boldsymbol{r}_{\mathrm{mean}}$. The ellipse radii correspond to the eigenvalues of the tensor of gyration. To enable clearer visualization, only $\boldsymbol{r}_{\mathrm{mean}}$ with carbon index of $i = 2n$ are shown and $R_{\alpha\beta}$ is also shown selectively (every other chain, two per chain) for the same reason.

Fig. 8 shows that the stearamide molecules become more upright, more extended (more separated $\boldsymbol{r}_{\mathrm{mean}}$), and less mobile (smaller $R_{\alpha\beta}$) as the surface coverage increases. These observations are in agreement with previous NEMD simulations[33] as well as QCM and ellipsometry experiments of a range of OFMs adsorbed on oxide surfaces.[20] At low Γ, the stearamide molecules adopt a flatter conformation to maximise van der Waals interactions between the tailgroups and the surfaces, as shown in previous DFT calculations.[46] At high Γ, van der Waals interactions between proximal tailgroups lead the molecules to adopt an upright, all-*trans* conformation, and only molecules directly underneath the tip contain gauche defects. In general, molecules located at the leading edge of the tip are deformed in the direction of sliding and stretched, while those at the trailing edge bend forward and form gauche defects around halfway up the tailgroup. Localised gauche defects at the trailing edge of the sliding tip were also observed in previous NEMD simulations of OTS SAMs.[41]

Fig. 8 shows the change in the configuration of the coarse-grained molecules as the tip moves forward ($+x$) by a unit spacing of Δx = bin size. Thus, the conformation of molecule j changes to that of molecule j-1 (molecule j-1 located on the left hand side of molecule j in Fig. 8) after a time interval, $\Delta\tau = \Delta x/v_x$. In that sense, Fig. 8 depicts a dynamic evolution of the film in response to the sliding tip, with each molecule in a nonequilibrium steady state. By comparing the configurations of a molecule at τ and $\tau+\Delta\tau$, one can measure the deviation of its position from a previous time frame: $\Delta\boldsymbol{r}(\Delta\tau) = \boldsymbol{r}_{j-1} - \boldsymbol{r}_j + \Delta x$. The location dependence of the molecular instability can be evaluated in terms of a temperature rise (ΔT = T-T_0) by assuming that $T \propto \boldsymbol{v}^2$, where $\boldsymbol{v} = \Delta\boldsymbol{r}/\Delta\tau$. More specifically, T is derived from $m(v_x^2 + v_z^2) = 2\ k_B\ T$, where m is the sum of the masses of the coarse-grained atoms in each bin, v_x and v_z are the velocities in the x and z directions, and k_B is Boltzmann's constant. Here T_0 = 300 K, *i.e.* the simulation temperature. Note that the purpose here is not to quantitatively determine the instantaneous temperature rise, but rather to show differences in thermal dissipation between the different monolayer coverages. This helps to demonstrate the connection between tip-induced changes in molecular morphology with dynamic instabilities within the molecules.

Fig. 9 shows a normalised percentage $\Delta T/T_0$ mapping for the aforementioned representative case. The mean positions of the coarse-grained carbon atoms are shown to relate the dissipation and changes to the conformation of the stearamide molecules. In the case of Γ = 2 nm^{-2}, ΔT is very small and is evenly distributed over the tip-monolayer contact area. When $\Gamma > 2$ nm^{-2}, ΔT becomes significant, and is localised predominantly towards the trailing edge of the tip. While ΔT becomes more localised as coverage increases, the magnitude of ΔT is greatest for the system with highest μ in Fig. 5 (Γ = 4 nm^{-2}). In all cases, ΔT is negligible at the molecule-surface interface due to efficient thermostatting. Looking at the coarse-grained atom positions in Fig. 9, the largest ΔT values correspond to where the molecules are most deformed from their undisturbed conformations. There is a strong propensity for those molecules to restore to their relaxed configurations and release

the accumulated energy, particularly at high coverage ($\Gamma = 5$ nm^{-2}). This process is energetically beneficial and helps to reduce the friction forces as the molecules at the trailing edge push the tip forwards to recover their all-*trans* conformations. This is evidenced by the negative forces at the trailing edge of the tip in Fig. 7, which have also been noted in previous NEMD studies.[38,39] This thermal dissipation is rather different to that observed in NEMD simulations of tips plowing through crystalline solid surfaces, where the temperature rise is localised at the leading edge of the tip.[74]

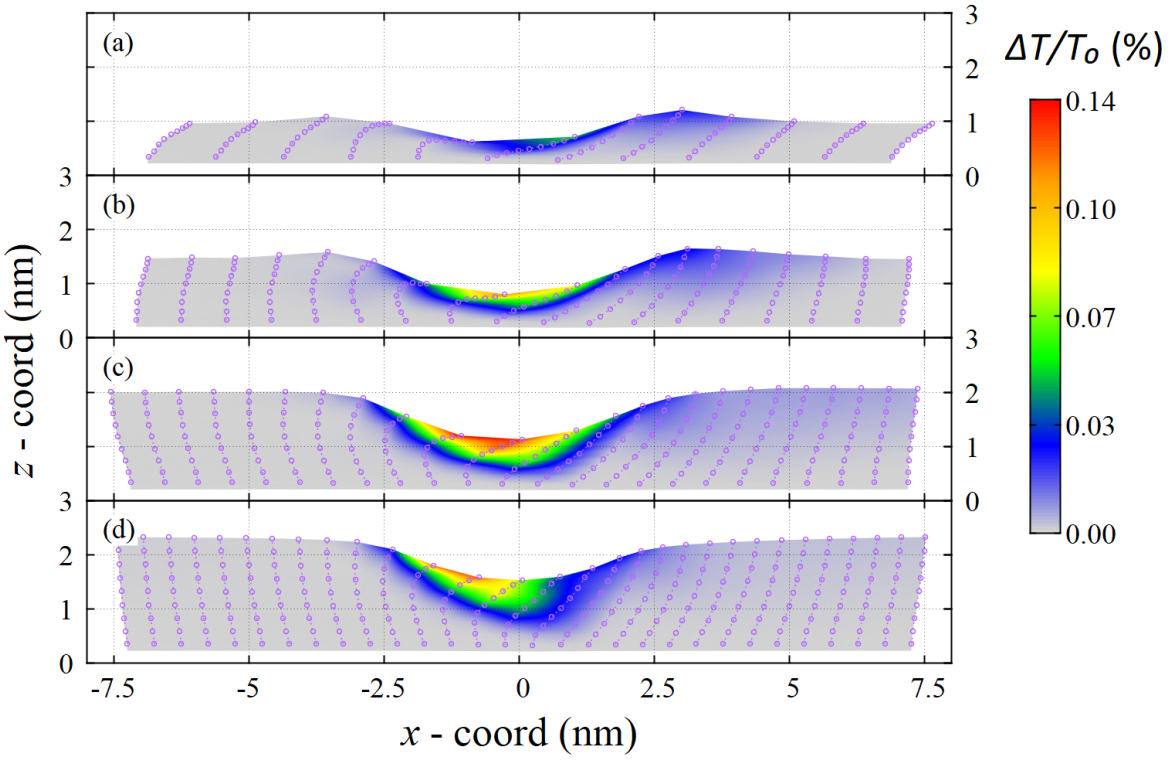

Figure 9: Effective relative temperature rise ($\Delta T/T_0$) for $r_{\text{tip}} = 4$ nm, $F_{\text{N}} = 30$ nN, and $\Gamma = 2$ nm^{-2} (a), 3 nm^{-2} (b), 4 nm^{-2} (c), and 5 nm^{-2} (d). Purple circles represent mean positions of tailgroup carbons projected onto the xz plane. To enable clearer visualization, only $\boldsymbol{r}_{\text{mean}}$ with carbon index of $i = 2n$ are shown. Sliding occurs in positive x-direction.

In the context of SAM friction, the nature of sliding-induced instabilities is surprisingly little investigated. Most NEMD studies consider two perfectly flat surfaces in sliding motion,[32,33] in which case viscoelastic deformation arising due to asperity collision or plowing

of a tip through a viscoelastic layer cannot occur. However, these additional dissipation mechanisms were identified as the predominant source of friction in asperity collisions of polymer brushes grafted to surfaces with nanoscale curvature.[81] Since the latter study was based on coarse-grained force fields, no typical molecular instabilities could occur, and thus no Coulomb-like friction regime was identified.[81] Elucidating Coulomb friction mechanisms thus entails identification of potential molecular instabilities. Towards this end, the positions of coarse-grained atoms were averaged in the x-direction within the frame of reference of the moving tip, as shown in Fig. 8. This reveals that coarse-grained molecules are bent into a curved shape at the leading edge in a quasi-continuous fashion, which is where large frictional stresses act on the tip, as evidenced in Fig. 7. At the trailing edge, deformed molecules snap back to their elongated all-*trans* conformation.

It could be argued that the temperature rise (Fig. 9) associated with these snaps is small, since the energies associated with the instabilities is < 1 % of the thermal energy. However, direct comparisons between the average temperature and the local temperature rise due to the instabilities may not be meaningful here for the following reasons. First, kinetic energy is measured at instantaneous times, while the positions of the coarse-grained atoms, and thus their velocities, are accrued over a 10 ps time scale. Second, the coarse-grained atoms move through a highly dissipate viscoelastic medium. Therefore, velocities corresponding to ≈ 0.1 % of the thermal velocities are actually quite considerable.

To substantiate our claim that the instabilities occur at the trailing edge of the moving tip, a sequence of simulations were conducted in which the tip was stopped and relaxed for 10 ps. The tip velocity was then reverted for a distance whose linear dimension equaled the bin size over which the atom configurations were shown in Fig. 8. The results, shown in Fig. 10, indicate that while coarsened molecule positions are recovered at the leading edge following velocity reversal, this is not the case for molecules at the trailing edge. This clearly reveals structural hysteresis of the molecules at the trailing edge of the tip. In summary, our results show that mechanical instabilities occur during sliding and strongly suggest that these are

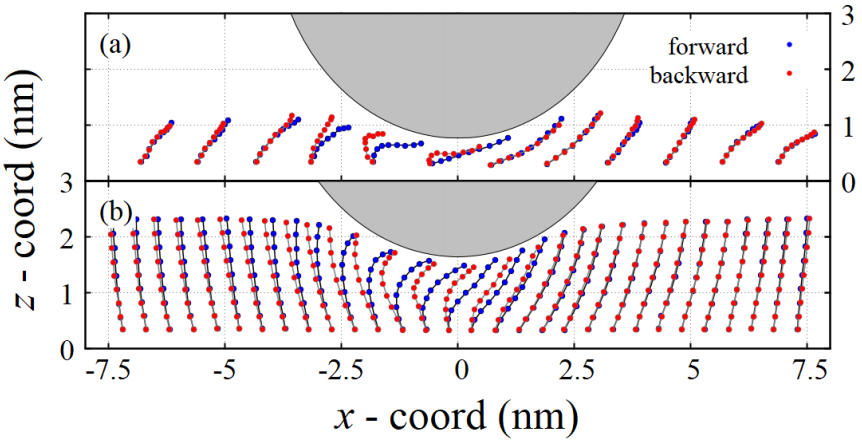

Figure 10: Coarse-grained molecular configurations from forward ($+x$, blue) and backward ($-x$, red) sliding in the cases of (a) $\Gamma = 2$ nm^{-2} and (b) $\Gamma = 5$ nm^{-2}, $r_{\mathrm{tip}} = 4$ nm, $F_{\mathrm{N}} = 30$ nN. To enable clearer visualization, only $\boldsymbol{r}_{\mathrm{mean}}$ with carbon index of $i = 2n$ are shown

the cause of velocity-independent friction (Fig. 6). This is consistent with the simple Prandtl model[85] that can account for the transition from Stokes to Coulomb friction.[84]

Conclusions

We have performed NEMD simulations using an all-atom force field to study frictional dissipation within OFM monolayers indented by sharp AFM tips. A wide range of surface coverages, tip radii, loads, sliding velocities were studied for stearamide monolayers chemisorbed on an α-Fe_2O_3 substrate, indented by an a-SiO_2 tip. For all the systems and conditions considered, there is measurable tip-monolayer indentation, and friction is dominated by molecular plowing. Even stearamide monolayers with low surface coverage are able to prevent direct solid-solid contact and withstand GPa-level local pressures applied by sharp tips and large loads. Friction forces increase linearly with normal force with finite intercepts, which can be adequately represented using Derjaguin's extension to Amonton's friction law. Sharper tips give larger friction coefficients (due to deeper indentation), but smaller Derjaguin offsets

(due to smaller contact area). A Coulomb-like relationship between friction and sliding velocity is observed, suggesting mechanical instabilities occur during sliding. Indeed, we show that while normal and shear stresses are localised at the leading edge of the tip, thermal dissipation occurs mostly at the trailing edge. More specifically, the sliding tip deforms the adsorbed molecules at its leading edge which snap back to their relaxed conformations at the trailing edge.

We have clarified the physical mechanisms driving the opposing friction-coverage relationships in nanoscale and macroscale experiments of OFMs. In macroscale tribometer experiments, and previous NEMD simulations with flat surfaces, friction decreases with increasing OFM surface coverage since this leads more solid-like monolayers and reduced interdigitation. For the current NEMD simulations with sharp nanoscale asperities that penetrate significantly into the OFM monolayers, non-monotonic friction-coverage behaviour is observed, which is due to a non-monotonic relationship between indentation depth and surface coverage. This, in turn, is due to the competing effects of increasing molecular packing density and decreasing confinement as the surface coverage is increased. Previous AFM experiments have either observed a decrease (for blunt tips) or increase (for sharp tips) in friction with increasing coverage. In future AFM experiments, we expect non-monotonic friction-coverage to be observable by using sharp tips and including OFMs that are known to form close-packed monolayer films.

Acknowledgement

H.G. thanks the Alexander von Humboldt Foundation for a Humboldt Research Fellowship. J.P.E. thanks the Royal Academy of Engineering for a Research Fellowship. J.P.E. and D.D. thank the Engineering and Physical Sciences Research Council (EPSRC) for an Established Career Fellowship EP/N025954/1 and grant EP/P030211/1. We thank Carlos Ayestarán Latorre for useful discussions. All data reported in the manuscript can be obtained by

emailing the corresponding author or tribology@imperial.ac.uk.

References

(1) Cheng, H. F.; Hu, Y. A. Influence of chain ordering on frictional properties of self-assembled monolayers (SAMs) in nano-lubrication. *Adv. Colloid Interface Sci.* **2012**, *171*, 53–65.

(2) Zhu, Y.; Free, M. L.; Woollam, R.; Durnie, W. A review of surfactants as corrosion inhibitors and associated modeling. *Prog. Mater. Sci.* **2017**, *90*, 159–223.

(3) Heinz, H.; Pramanik, C.; Heinz, O.; Ding, Y.; Mishra, R. K.; Marchon, D.; Flatt, R. J.; Estrela-Lopis, I.; Llop, J.; Moya, S.; Ziolo, R. F. Nanoparticle decoration with surfactants: Molecular interactions, assembly, and applications. *Surf. Sci. Rep.* **2017**, *72*, 1–58.

(4) Spikes, H. Friction Modifier Additives. *Tribol. Lett.* **2015**, *60*, 5.

(5) Taylor, R. I. Tribology and energy efficiency: from molecules to lubricated contacts to complete machines. *Faraday Discuss.* **2012**, *156*, 361–382.

(6) Hardy, W. B.; Doubleday, I. Boundary lubrication - The paraffin series. *Proc. R. Soc. London, Ser. A* **1922**, *100*, 550–557.

(7) Bowden, F.; Leben, L. The Friction of Lubricated Metals. *Philos. Trans. R. Soc. London, Ser. A* **1940**, *239*, 1–27.

(8) Blodgett, K. B. Films Built by Depositing Successive Monomolecular Layers on a Solid Surface. *J. Am. Chem. Soc.* **1935**, *57*, 1007–1022.

(9) Ulman, A. Formation and structure of self-assembled monolayers. *Chem. Rev.* **1996**, *96*, 1533–1554.

(10) Spikes, H. A.; Cameron, A. A comparison of adsorption and boundary lubricant failure. *Proc. Roy. Soc. Lond. A.* **1974**, *336*, 407–419.

(11) Jahanmir, S.; Beltzer, M. An adsorption model for friction in boundary lubrication. *ASLE Trans.* **1986**, *29*, 423–430.

(12) Jahanmir, S.; Beltzer, M. Effect of Additive Molecular-Structure on Friction Coefficient and Adsorption. *J. Tribol.* **1986**, *108*, 109–116.

(13) Jaishankar, A.; Jusufi, A.; Vreeland, J. L.; Deighton, P.; Pellettiere, J. R.; Schilowitz, A. M. Adsorption of stearic acid at the iron oxide/oil interface - theory, experiments and modeling. *Langmuir* **2019**, *35*, 2033–2046.

(14) Szlufarska, I.; Chandross, M.; Carpick, R. W. Recent advances in single-asperity nanotribology. *J. Phys. D: Appl. Phys.* **2008**, *41*, 123001.

(15) Simič, R.; Kalin, M. Adsorption mechanisms for fatty acids on DLC and steel studied by AFM and tribological experiments. *Appl. Surf. Sci.* **2013**, *283*, 460–470.

(16) Campen, S.; Green, J. H.; Lamb, G. D.; Spikes, H. A. In Situ Study of Model Organic Friction Modifiers Using Liquid Cell AFM: Self-Assembly of Octadecylamine. *Tribol. Lett.* **2015**, *58*, 39.

(17) Campen, S.; Green, J. H.; Lamb, G. D.; Spikes, H. A. In Situ Study of Model Organic Friction Modifiers Using Liquid Cell AFM; Saturated and Mono-unsaturated Carboxylic Acids. *Tribol. Lett.* **2015**, *57*, 18.

(18) Ruths, M.; Lundgren, S.; Danerlov, K.; Persson, K. Friction of fatty acids in nanometer-sized contacts of different adhesive strength. *Langmuir* **2008**, *24*, 1509–1516.

(19) Nalam, P. C.; Pham, A.; Castillo, R. V.; Espinosa-Marzal, R. M. Adsorption Behavior and Nanotribology of Amine-Based Friction Modifiers on Steel Surfaces. *J. Phys. Chem. C* **2019**, *123*, 13672–13680.

(20) Fry, B. M.; Moody, G.; Spikes, H. A.; Wong, J. S. S. Adsorption of Organic Friction Modifier Additives. *Langmuir* **2020**, *36*, 1147–1155.

(21) Xiao, X.; Hu, J.; Charych, D. H.; Salmeron, M. Chain Length Dependence of the Frictional Properties of Alkylsilane Molecules Self-Assembled on Mica Studied by Atomic Force Microscopy. *Langmuir* **1996**, *12*, 235–237.

(22) Lio, A.; Charych, D. H.; Salmeron, M. Comparative atomic force microscopy study of the chain length dependence of frictional properties of alkanethiols on gold and alkylsilanes on Mica. *J. Phys. Chem. B* **1997**, *101*, 3800–3805.

(23) McDermott, M. T.; Green, J.-B. D.; Porter, M. D. Scanning Force Microscopic Exploration of the Lubrication Capabilities of n-Alkanethiolate Monolayers Chemisorbed at Gold: Structural Basis of Microscopic Friction and Wear. *Langmuir* **1997**, *13*, 2504–2510.

(24) Lee, S.; Shon, Y.-S.; Colorado, R.; Guenard, R. L.; Lee, T. R.; Perry, S. S. The Influence of Packing Densities and Surface Order on the Frictional Properties of Alkanethiol Self-Assembled Monolayers (SAMs) on Gold: A Comparison of SAMs Derived from Normal and Spiroalkanedithiols. *Langmuir* **2000**, *16*, 2220–2224.

(25) Shon, Y. S.; Lee, S.; Colorado, R.; Perry, S. S.; Lee, T. R. Spiroalkanedithiol-based SAMs reveal unique insight into the wettabilities and frictional properties of organic thin films. *J. Am. Chem. Soc.* **2000**, *122*, 7556–7563.

(26) Foster, T. T.; Alexander, M. R.; Leggett, G. J.; McAlpine, E. Friction force microscopy of alkylphosphonic acid and carboxylic acids adsorbed on the native oxide of aluminum. *Langmuir* **2006**, *22*, 9254–9259.

(27) Brukman, M. J.; Marco, G. O.; Dunbar, T. D.; Boardman, L. D.; Carpick, R. W. Nanotribological Properties of Alkanephosphonic Acid Self-Assembled Monolayers on

Aluminum Oxide: Effects of Fluorination and Substrate Crystallinity. *Langmuir* **2006**, *22*, 3988–3998.

(28) Flater, E. E.; Ashurst, W. R.; Carpick, R. W. Nanotribology of octadecyltrichlorosilane monolayers and silicon: Self-mated versus unmated interfaces and local packing density effects. *Langmuir* **2007**, *23*, 9242–9252.

(29) Yang, Y.; Ruths, M. Friction of Polyaromatic Thiol Monolayers in Adhesive and Non-adhesive Contacts. *Langmuir* **2009**, *1894*, 12151–12159.

(30) Yang, Y.; Singh, J.; Ruths, M. Friction of aromatic thiol monolayers on silver: SFA and AFM studies of adhesive and non-adhesive. *RSC Adv.* **2014**, *4*, 18801–18810.

(31) Ewen, J. P.; Heyes, D. M.; Dini, D. Advances in nonequilibrium molecular dynamics simulations of lubricants and additives. *Friction* **2018**, *6*, 349–386.

(32) Doig, M.; Warrens, C. P.; Camp, P. J. Structure and friction of stearic acid and oleic acid films adsorbed on iron oxide surfaces in squalane. *Langmuir* **2014**, *30*, 186–195.

(33) Ewen, J. P.; Gattinoni, C.; Morgan, N.; Spikes, H. A.; Dini, D. Nonequilibrium Molecular Dynamics Simulations of Organic Friction Modifiers Adsorbed on Iron Oxide Surfaces. *Langmuir* **2016**, *32*, 4450.

(34) Eder, S. J.; Vernes, A.; Betz, G. On the Derjaguin Offset in Boundary-Lubricated Nanotribological Systems. *Langmuir* **2013**, *29*, 13760–13772.

(35) Ewen, J. P.; Echeverri Restrepo, S.; Morgan, N.; Dini, D. Nonequilibrium molecular dynamics simulations of stearic acid adsorbed on iron surfaces with nanoscale roughness. *Tribol. Int.* **2017**, *107*, 264–273.

(36) Campen, S.; Green, J.; Lamb, G.; Atkinson, D.; Spikes, H. On the increase in boundary friction with sliding speed. *Tribol. Lett.* **2012**, *48*, 237–248.

(37) Wood, M. H.; Casford, M. T.; Steitz, R.; Zarbakhsh, A.; Welbourn, R. J. L.; Clarke, S. M. Comparative Adsorption of Saturated and Unsaturated Fatty Acids at the Iron Oxide/Oil Interface. *Langmuir* **2016**, *32*, 534.

(38) Knippenberg, M. T.; Mikulski, P. T.; Dunlap, B. I.; Harrison, J. A. Atomic contributions to friction and load for tip-self-assembled monolayers interactions. *Phys. Rev. B* **2008**, *78*, 235409.

(39) Knippenberg, M. T.; Mikulski, P. T.; Harrison, J. A. Effects of tip geometry on interfacial contact forces. *Model. Simul. Mater. Sci. Eng.* **2010**, *18*, 034002.

(40) Chandross, M.; Lorenz, C. D.; Stevens, M. J.; Grest, G. S. Simulations of nanotribology with realistic probe tip models. *Langmuir* **2008**, *24*, 1240–1246.

(41) Summers, A. Z.; Iacovella, C. R.; Cummings, P. T.; McCabe, C. Investigating Alkylsilane Monolayer Tribology at a Single-Asperity Contact with Molecular Dynamics Simulation. *Langmuir* **2017**, *33*, 11270–11280.

(42) Raider, S. I.; Flitsch, R.; Aboaf, J. A.; Pliskin, W. A. Surface Oxidation of Silicon Nitride Films. *J. Electrochem. Soc.* **1976**, *123*, 560–565.

(43) Luan, B. Q.; Robbins, M. O. The breakdown of continuum models for mechanical contacts. *Nature* **2005**, *435*, 929–932.

(44) de Beer, S.; den Otter, W. K.; van den Ende, D.; Briels, W. J.; Mugele, F. Can confinement-induced variations in the viscous dissipation be measured? *Tribol. Lett.* **2012**, *48*, 1–9.

(45) Oh, S. J.; Cook, D. C.; Townsend, H. E. Characterization of iron oxides commonly formed as corrosion products on steel. *Hyperfine Interact.* **1998**, *112*, 59–66.

(46) Gattinoni, C.; Ewen, J. P.; Dini, D. Adsorption of Surfactants on α-Fe2O3(0001): A Density Functional Theory Study. *J. Phys. Chem. C* **2018**, *122*, 20817–20826.

(47) Humphrey, W.; Dalke, A.; Schulten, K. VMD: Visual molecular dynamics. *J. Mol. Graph. Model.* **1996**, *14*, 33–38.

(48) Ingram, M.; Noles, J.; Watts, R.; Harris, S.; Spikes, H. A. Frictional Properties of Automatic Transmission Fluids: Part I-Measurement of Friction-Sliding Speed Behavior. *Tribol. Trans.* **2011**, *54*, 145–153.

(49) Briscoe, B. J.; Mustafaev, V.; Tabor, D. Lubrication of polythene by oleamide and stearamide. *Wear* **1972**, *19*, 399–414.

(50) Ramirez, M. X.; Hirt, D. E.; Wright, L. L. AFM Characterization of Surface Segregated Erucamide and Behenamide in Linear Low Density Polyethylene Film. *Nano Lett.* **2002**, *2*, 9–12.

(51) Wood, M. H.; Welbourn, R. J. L.; Charlton, T.; Zarbakhsh, A.; Casford, M. T.; Clarke, S. M. Hexadecylamine Adsorption at the Iron Oxide-Oil Interface. *Langmuir* **2013**, *29*, 13735–13742.

(52) Lundgren, S. M.; Persson, K.; Mueller, G.; Kronberg, B.; Clarke, J.; Chtaib, M.; Claesson, P. M. Unsaturated fatty acids in alkane solution: adsorption to steel surfaces. *Langmuir* **2007**, *23*, 10598–10602.

(53) Xing, W.; Shan, Y.; Guo, D.; Lu, T.; Xi, S. Mechanism of iron inhibition by stearic acid Langmuir-Blodgett monolayers. *Corrosion* **1995**, *51*, 45–49.

(54) Jorgensen, W. L.; Maxwell, D. S.; Tirado-Rives, J. Development and testing of the OPLS all-atom force field on conformational energetics and properties of organic liquids. *J. Am. Chem. Soc.* **1996**, *118*, 11225–11236.

(55) Siu, S. W. I.; Pluhackova, K.; Bockmann, R. A. Optimization of the OPLS-AA Force Field for Long Hydrocarbons. *J. Chem. Theory Comput.* **2012**, *8*, 1459–1470.

(56) Ewen, J. P.; Gattinoni, C.; Thakkar, F. M.; Morgan, N.; Spikes, H.; Dini, D. A Comparison of Classical Force-Fields for Molecular Dynamics Simulations of Lubricants. *Materials.* **2016**, *9*, 651.

(57) Blake, R. L.; Hessevick, R. E.; Finger, L. W. Refinement of the Hematite Structure. *Am. Mineral.* **1966**, *51*, 123–129.

(58) Berro, H.; Fillot, N.; Vergne, P. Molecular dynamics simulation of surface energy and ZDDP effects on friction in nano-scale lubricated contacts. *Tribol. Int.* **2010**, *43*, 1811–1822.

(59) Ayestarán Latorre, C.; Ewen, J. P.; Gattinoni, C.; Dini, D. Simulating Surfactant-Iron Oxide Interfaces: From Density Functional Theory to Molecular Dynamics. *J. Phys. Chem. B* **2019**, *123*, 6870–6881.

(60) van Beest, B. W. H.; Kramer, G. J.; van Santen, R. A. Force Fields for Silicas and Aluminophosphates Based on Ab Initio Calculations. *Phys. Rev. Lett.* **1990**, *64*, 1955–1958.

(61) Döpke, M. F.; Lutzenkirchen, J.; Moultos, O. A.; Siboulet, B.; Dufreche, J.-F.; Padding, J. T.; Hartkamp, R. Preferential Adsorption in Mixed Electrolytes Confined by Charged Amorphous Silica. *J. Phys. Chem. C* **2019**, *123*, 16711–16720.

(62) Yeh, I. C.; Berkowitz, M. L. Ewald summation for systems with slab geometry. *J. Chem. Phys.* **1999**, *111*, 3155–3162.

(63) Plimpton, S. Fast Parallel Algorithms for Short-Range Molecular Dynamics. *J. Comput. Phys.* **1995**, *117*, 1 – 19.

(64) Schneider, T.; Stoll, E. Molecular-dynamics study of a three-dimensional one-component model for distortive phase-transitions. *Phys. Rev. B* **1978**, *17*, 1302–1322.

(65) Bernardi, S.; Todd, B. D.; Searles, D. J. Thermostating highly confined fluids. *J. Chem. Phys.* **2010**, *132*, 244706.

(66) Yong, X.; Zhang, L. T. Thermostats and thermostat strategies for molecular dynamics simulations of nanofluidics. *J. Chem. Phys.* **2013**, *138*, 084503.

(67) Sam, A.; Kannam, S. K.; Hartkamp, R.; Sathian, S. P. Water flow in carbon nanotubes: The effect of tube flexibility and thermostat. *J. Chem. Phys.* **2017**, *146*, 234701.

(68) Chandross, M.; Lorenz, C. D.; Grest, G. S.; Stevens, M. J.; Webb III, E. B. Nanotribology of Anti-Friction Coatings in MEMS. *JOM* **2005**, *57*, 55–61.

(69) Taylor, R. I.; de Kraker, B. R. Shear rates in engines and implications for lubricant design. *Proc. Inst. Mech. Eng. Part J.* **2017**, *231*, 1106–1116.

(70) Echeverri Restrepo, S.; van Eijk, M. C. P.; Ewen, J. P. Behaviour of n-alkanes confined between iron oxide surfaces at high pressure and shear rate: A nonequilibrium molecular dynamics study. *Tribol. Int.* **2019**, *137*, 420–432.

(71) Jabbarzadeh, A. Friction anisotropy and asymmetry in self assembled monolayers. *Tribol. Int.* **2016**, *102*, 600–607.

(72) Salmeron, M.; Neubauer, G.; Folch, A.; Tomitori, M.; Ogletree, D. F.; Sautet, P. Viscoelastic and Electrical Properties of Self-Assembled Monolayers on Au(111) Films. *Langmuir* **1993**, *9*, 3600–3611.

(73) Gao, Y.; Brodyanski, A.; Kopnarski, M.; Urbassek, H. M. Nanoscratching of iron: A molecular dynamics study of the influence of surface orientation and scratching direction. *Comput. Mater. Sci.* **2015**, *103*, 77–89.

(74) Stephan, S.; Dyga, M.; Urbassek, H. M.; Hasse, H. The Influence of Lubrication and the Solid-Fluid Interaction on Thermodynamic Properties in a Nanoscopic Scratching Process. *Langmuir* **2019**, *35*, 16948–16960.

(75) Houston, J. E.; Kim, H. I. Adhesion, friction, and mechanical properties of functionalized alkanethiol self-assembled monolayers. *Acc. Chem. Res.* **2002**, *35*, 547–553.

(76) Salmeron, M. Generation of defects in model lubricant monolayers and their contribution to energy dissipation in friction. *Tribol. Lett.* **2001**, *10*, 69–79.

(77) Gao, H.; Müser, M. H. Why liquids can appear to solidify during squeeze-out - even when they don't. *J. Colloid Interface Sci.* **2020**, *562*, 273–278.

(78) Derjaguin, B. Molekulartheorie der äuβeren Reibung. *Z. Phys. A* **1934**, *88*, 661–675.

(79) Briscoe, B. J.; Evans, D. C. B. The shear properties of Langmuir-Blodgett layers. *Proc. R. Soc. London, Ser. A* **1982**, *380*, 389–407.

(80) Brewer, N. J.; Beake, B. D.; Leggett, G. J. Friction force microscopy of self-assembled monolayers: Influence of adsorbate alkyl chain length, terminal group chemistry, and scan velocity. *Langmuir* **2001**, *17*, 1970–1974.

(81) de Beer, S.; Müser, M. H. Alternative dissipation mechanisms and the effect of the solvent in friction between polymer brushes on rough surfaces. *Soft Matter* **2013**, *9*, 7234–7241.

(82) Ouyang, W.; de Wijn, A. S.; Urbakh, M. Atomic-scale sliding friction on a contaminated surface. *Nanoscale* **2018**, *10*, 6375–6381.

(83) Yoshizawa, H.; Chen, Y. L.; Israelachvili, J. Fundamental mechanisms of interfacial friction. 1. relation between adhesion and friction. *J. Phys. Chem.* **1993**, *97*, 4128–4140.

(84) Müser, M. H. Nature of Mechanical Instabilities and Their Effect on Kinetic Friction. *Phys. Rev. Lett.* **2002**, *89*, 224301.

(85) Prandtl, L. Ein Gedankenmodell zur kinetischen Theorie der festen Körper. *Z. Angew. Math. Mech.* **1928**, *8*, 85–106.

(86) Müser, M. H. Shear Thinning in the Prandtl Model and Its Relation to Generalized Newtonian Fluids. *Lubricants* **2020**, *8*, 38.

(87) Li, Q. Y.; Dong, Y. L.; Perez, D.; Martini, A.; Carpick, R. W. Speed Dependence of Atomic Stick-Slip Friction in Optimally Matched Experiments and Molecular Dynamics Simulations. *Phys. Rev. Lett.* **2011**, *106*, 126101.

(88) Wenning, L.; Müser, M. H. Friction laws for elastic nanoscale contacts. *Europhys. Lett.* **2001**, *54*, 693.

(89) Ewers, B. W.; Batteas, J. D. Utilizing Atomistic Simulations To Map Pressure Distributions and Contact Areas in Molecular Adlayers within Nanoscale Surface-Asperity Junctions: A Demonstration with Octadecylsilane-Functionalized Silica Interfaces. *Langmuir* **2014**, *30*, 11897–11905.

(90) Ma, E. Instabilities and ductility of nanocrystalline and ultrafine-grained metals. *Scr. Mater.* **2003**, *49*, 663–668.

(91) Persson, B. N. J. Theory of rubber friction and contact mechanics. *J. Chem. Phys.* **2001**, *115*, 3840–3861.

Graphical TOC Entry